





RESEARCH ARTICLE | MAY 11 2026

# Phase-selective sputter epitaxy of $\delta$ -NbN, $\gamma$ -Nb<sub>4</sub>N<sub>3</sub>, and $\beta$ -Nb<sub>2</sub>N on atomically flat AlN

Special Collection: [Frontiers in Nitride Semiconductors Research](#)Yuki Kato ; Koryo Masuzawa ; Takayuki Harada ; Hideto Miyake ; Atsushi Kobayashi  *J. Appl. Phys.* 139, 185301 (2026)<https://doi.org/10.1063/5.0311297>View  
OnlineExport  
Citation

## Articles You May Be Interested In

rf reactively sputtered superconducting NbN<sub>x</sub> films*J. Appl. Phys.* (July 1974)

Pulsed laser deposition of niobium nitride thin films

*AIP Conf. Proc.* (December 2015)Transition temperatures and crystal structures of single-crystal and polycrystalline NbN<sub>x</sub> films*J. Appl. Phys.* (March 1974)

## AIP Advances

### Why Publish With Us?

**21DAYS**  
average time  
to 1st decision**OVER 4 MILLION**  
views in the last year**INCLUSIVE**  
scope[Learn More](#)

# Phase-selective sputter epitaxy of $\delta$ -NbN, $\gamma$ -Nb<sub>4</sub>N<sub>3</sub>, and $\beta$ -Nb<sub>2</sub>N on atomically flat AlN

Cite as: J. Appl. Phys. **139**, 185301 (2026); doi: [10.1063/5.0311297](https://doi.org/10.1063/5.0311297)

Submitted: 8 November 2025 · Accepted: 21 April 2026 ·

Published Online: 11 May 2026



Yuki Kato,<sup>1</sup> , Koryo Masuzawa,<sup>1</sup> , Takayuki Harada,<sup>1,2</sup> , Hideto Miyake,<sup>3,4</sup> and Atsushi Kobayashi<sup>1,a)</sup>

## AFFILIATIONS

<sup>1</sup>Department of Materials Science and Technology, Tokyo University of Science, Tokyo 125-8585, Japan

<sup>2</sup>MANA, National Institute for Materials Science, Ibaraki 305-0044, Japan

<sup>3</sup>Graduate School of Engineering, Mie University, Mie 514-8507, Japan

<sup>4</sup>Innovation Center for Semiconductor and Digital Future, Mie University, Mie 514-8507, Japan

**Note:** This paper is part of the Special Topic on Frontiers in Nitride Semiconductors Research.

<sup>a)</sup>Author to whom correspondence should be addressed: [akoba@rs.tus.ac.jp](mailto:akoba@rs.tus.ac.jp)

## ABSTRACT

We report the phase-selective epitaxy of  $\delta$ -NbN,  $\gamma$ -Nb<sub>4</sub>N<sub>3</sub>, and  $\beta$ -Nb<sub>2</sub>N thin films on AlN/sapphire templates by sputtering. Structural analysis revealed coherent epitaxial growth with sharp x-ray diffraction fringes, phase-dependent surface reconstructions observed by reflection high-energy electron diffraction, and atomically flat morphologies with a root-mean-square roughness below 1 nm. Reciprocal space mapping confirmed lattice coherence, while rocking curves exhibited narrow full width at half maximum values for  $\delta$ -NbN and  $\beta$ -Nb<sub>2</sub>N, with slightly broader peaks for  $\gamma$ -Nb<sub>4</sub>N<sub>3</sub>. Transport measurements showed distinct superconducting behaviors:  $\delta$ -NbN displayed an insulating-like resistivity upturn with  $T_c \sim 12$  K,  $\gamma$ -Nb<sub>4</sub>N<sub>3</sub> exhibited metallic behavior with  $T_c \sim 10$  K, and  $\beta$ -Nb<sub>2</sub>N showed metallic conduction with  $T_c$  as low as 0.4 K, indicating high phase purity. The retention of high  $T_c$  values in ultrathin films underscores the robustness of sputter-grown NbN<sub>x</sub> on AlN. These results define the growth windows for multiple NbN<sub>x</sub> phases and establish AlN as a versatile platform for integrating superconductivity with III-nitride semiconductors in future hybrid devices.

© 2026 Author(s). All article content, except where otherwise noted, is licensed under a Creative Commons Attribution (CC BY) license (<https://creativecommons.org/licenses/by/4.0/>). <https://doi.org/10.1063/5.0311297>

## I. INTRODUCTION

Niobium nitride (NbN<sub>x</sub>) has long attracted attention as a superconducting material due to its relatively high critical temperature ( $T_c \sim 17$ – $18$  K for  $\delta$ -NbN),<sup>1</sup> short coherence length ( $\xi \approx 4$ – $7$  nm),<sup>2</sup> mechanical robustness,<sup>3,4</sup> and chemical stability.<sup>5</sup> Owing to these favorable properties, NbN<sub>x</sub> is widely explored for applications in superconducting qubits,<sup>6,7</sup> single-photon detectors,<sup>8,9</sup> and hot-electron bolometers.<sup>10,11</sup> However, the performance of these devices is highly sensitive to the crystalline phase and structural homogeneity of the NbN<sub>x</sub> films. The spontaneous formation of multiple polymorphs during growth can introduce local variations in the  $T_c$  and magnetic penetration depth, which lead to increased noise in detectors and reduced coherence times in quantum circuits. Since the discovery of superconductivity in NbN in 1941,<sup>12</sup> numerous studies have revealed that NbN<sub>x</sub> forms several crystal polymorphs in addition to the stable rocksalt

$\delta$ -NbN phase, including  $\gamma$ -Nb<sub>4</sub>N<sub>3</sub>,<sup>13</sup>  $\beta$ -Nb<sub>2</sub>N,<sup>14–16</sup>  $\epsilon$ -NbN,<sup>4</sup> and others.<sup>17,18</sup> These polymorphs exhibit markedly different superconducting transition temperatures, yet systematic investigations of epitaxial single-crystal films remain limited, leaving the relationship between crystal phase, structural coherence, and superconducting properties unresolved.

The epitaxial growth of NbN<sub>x</sub> has been demonstrated on MgO<sup>19,20</sup> and SiC<sup>21,22</sup> substrates, with lattice mismatches of approximately 4.3% and 0.7% for  $\delta$ -NbN, respectively. However, group-III nitrides such as AlN<sup>8,23,24</sup> and GaN<sup>25–29</sup> offer distinct advantages: They provide even closer lattice compatibility with NbN<sub>x</sub> ( $-0.2\%$  for  $\delta$ -NbN/AlN and  $2.7\%$  for  $\delta$ -NbN/GaN), while also enabling mature device technologies and supporting high breakdown fields. This combination makes III-nitrides attractive platforms for superconductor–semiconductor integration. Notably, GaN/NbN heterostructures have been reported to host

two-dimensional electron gases,<sup>27,30</sup> underscoring the potential for combining superconductivity with III-nitride functionalities.

Despite their promise, reports on the epitaxial growth of distinct NbN<sub>x</sub> phases on AlN remain scarce, and their structural and superconducting characteristics are not yet well understood. Establishing a growth window that allows for the selective stabilization of a single NbN<sub>x</sub> phase on AlN is therefore essential for eliminating the detrimental effects of phase coexistence and for the realization of high-performance hybrid quantum devices. In this work, we demonstrate the phase-selective sputter epitaxy of  $\delta$ -NbN,  $\gamma$ -Nb<sub>4</sub>N<sub>3</sub>, and  $\beta$ -Nb<sub>2</sub>N thin films on atomically flat AlN/sapphire templates. The surface morphology, crystalline quality, and superconducting transport properties of these films were systematically characterized, establishing the growth windows for each phase and providing a foundation for future superconductor–semiconductor hybrid devices.

## II. EXPERIMENTAL

Epitaxial NbN<sub>x</sub> thin films were grown on AlN/sapphire templates consisting of a 200 nm-thick AlN layer deposited by sputtering and subsequently annealed in a face-to-face configuration at 1700 °C,<sup>31</sup> followed by the growth of a 160 nm-thick AlN homoepitaxial cap layer by metalorganic vapor phase epitaxy. The resulting AlN templates exhibited an in-plane lattice constant of  $\sim 3.09$  Å and x-ray rocking curve (XRC) measurements yielded full width at half maximum (FWHM) values of 10–12 arc sec for the (0002) reflection and 240–260 arc sec for the (10 $\bar{1}2$ ) reflection. DC-pulsed sputtering was carried out using a 2 in. Nb target (99.9%) at a base pressure  $\sim 10^{-8}$  Pa. To control the phase-selective growth, the gas chemistry and pulsing parameters were optimized for each phase. For  $\delta$ -NbN and  $\gamma$ -Nb<sub>4</sub>N<sub>3</sub>, pure N<sub>2</sub> was introduced (Ar:N<sub>2</sub> = 0:100 SCCM) at a total pressure of 2.7 Pa, with a pulse frequency of  $\sim 4.2$  kHz and a pulse-on time of 40  $\mu$ s (duty cycle  $\sim 17\%$ ). For  $\beta$ -Nb<sub>2</sub>N, the nitrogen partial pressure ( $P_{N_2}$ ) was reduced to 0.5% using an Ar:N<sub>2</sub> ratio of 400:2 SCCM at a total pressure of 0.54 Pa, with a pulse frequency of 5 kHz and a 4  $\mu$ s pulse width (duty cycle 2%). The  $P_{N_2}$  was drastically reduced to 0.5% for  $\beta$ -Nb<sub>2</sub>N growth to achieve the required substoichiometry, as the  $\beta$  phase is only stable under very low nitrogen chemical potentials compared to the  $\delta$  and  $\gamma$  phases.<sup>24,32</sup> The pulse powers were set to 50–55 W. Substrate temperatures of 800, 1000, or 1100 °C were employed, and the resulting film thicknesses ranged from 5 to 25 nm. Phase selection was achieved by simultaneously tuning the substrate temperature and nitrogen partial pressure via these optimized pulsing and gas-flow conditions.

Structural and surface characterizations were performed using high-resolution x-ray diffraction ( $2\theta/\omega$  scans and symmetric/asymmetric reciprocal space mapping), reflection high-energy electron diffraction, and atomic force microscopy. The superconducting transport properties were evaluated by low-temperature four-probe resistivity measurements in a <sup>3</sup>He cryostat. Indium electrodes were deposited on the samples and connected to the measurement probe with gold wires.  $T_c$  was defined as the temperature corresponding to 50% of the normal-state resistance. Magnetic-field-dependent measurements were conducted using a physical property measurement system (PPMS).

## III. RESULTS AND DISCUSSION

X-ray diffraction  $2\theta/\omega$  scans (Fig. 1) revealed the phase-selective epitaxy of NbN<sub>x</sub> on AlN/sapphire. The diffraction peak positions systematically shifted with growth conditions, enabling identification of the corresponding crystalline phases. Under N<sub>2</sub>-rich conditions ( $P_{N_2} = 100\%$ ), increasing the substrate temperature transformed the phase from  $\delta$ -NbN at 800 °C to  $\gamma$ -Nb<sub>4</sub>N<sub>3</sub> at 1100 °C, consistent with previous reports by Kobayashi *et al.*<sup>24</sup> and Wright *et al.*<sup>32</sup> In contrast, reducing the N<sub>2</sub> fraction to 0.5% at 1000 °C stabilized  $\beta$ -Nb<sub>2</sub>N, which has not been previously reported for sputter epitaxy. All films exhibited sharp diffraction peaks with pronounced interference fringes, confirming coherent epitaxy on the AlN/sapphire templates. XRC measurements were performed to assess the crystalline quality of  $\delta$ -NbN,  $\gamma$ -Nb<sub>4</sub>N<sub>3</sub>, and  $\beta$ -Nb<sub>2</sub>N films. Tilt components were analyzed using the (111) reflection for  $\delta$ -NbN, (112) for  $\gamma$ -Nb<sub>4</sub>N<sub>3</sub>, and (0002) for  $\beta$ -Nb<sub>2</sub>N. All films showed narrow full FWHM below 400 arc sec, with  $\delta$ -NbN exhibiting the sharpest peak. The XRC FWHM values below 400 arc sec for all films indicate high crystalline quality across the investigated thickness range. Twist components were evaluated using the (002) reflection for  $\delta$ -NbN, (004) for  $\gamma$ -Nb<sub>4</sub>N<sub>3</sub>, and (10 $\bar{1}2$ ) for  $\beta$ -Nb<sub>2</sub>N.  $\delta$ -NbN and  $\beta$ -Nb<sub>2</sub>N exhibited FWHM values below 800 arc sec, whereas  $\gamma$ -Nb<sub>4</sub>N<sub>3</sub> exceeded 1000 arc sec, indicating reduced in-plane coherence. To contextualize these results, a quantitative comparison with previously reported FWHM values for epitaxial NbN<sub>x</sub> films grown by various methods and on different substrates is provided in Table S1 in the [supplementary material](#). Our sputtered films exhibit crystallinity

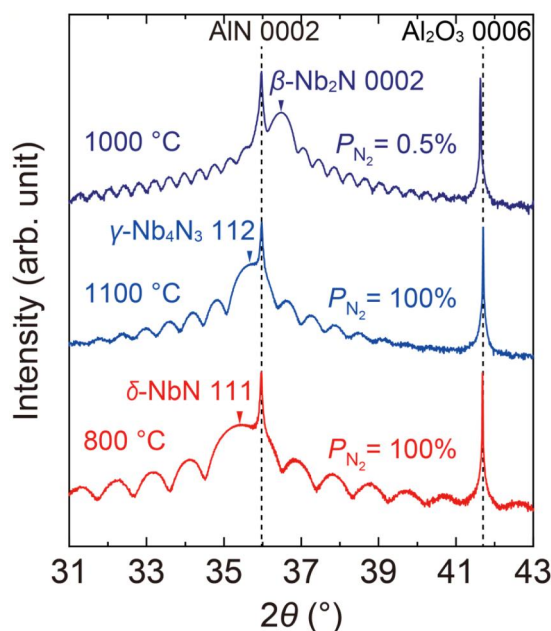
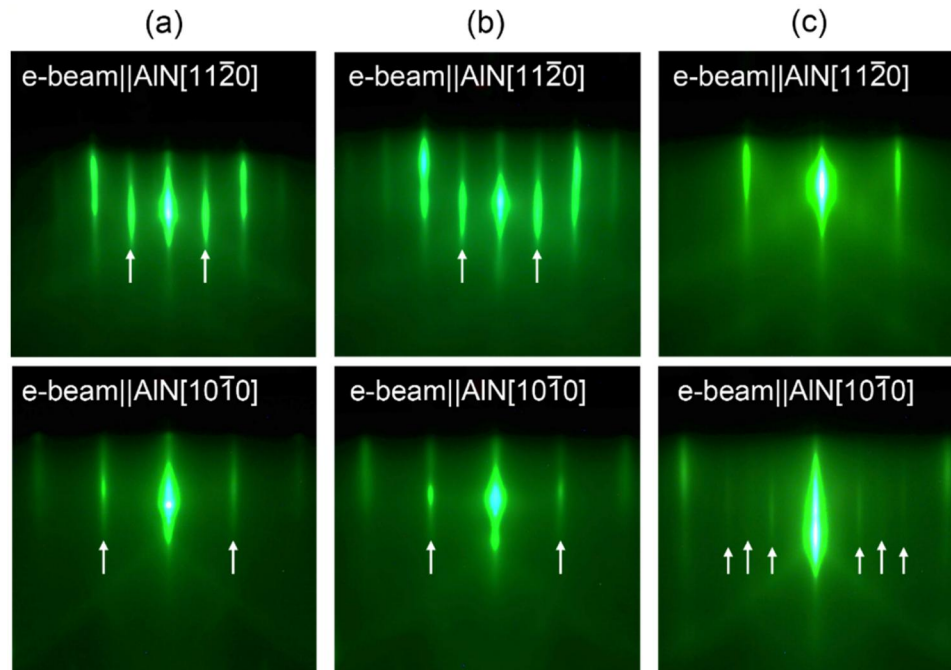


FIG. 1. XRD  $2\theta$  scans of  $\delta$ -NbN,  $\gamma$ -Nb<sub>4</sub>N<sub>3</sub>, and  $\beta$ -Nb<sub>2</sub>N epitaxially grown on AlN. The growth temperature and N<sub>2</sub> partial pressure ( $P_{N_2}$ ) are indicated.



**FIG. 2.** RHEED patterns of (a)  $\delta$ -NbN, (b)  $\gamma$ -Nb<sub>4</sub>N<sub>3</sub>, and (c)  $\beta$ -Nb<sub>2</sub>N films grown on AlN, recorded along the AlN[112̄0] and [101̄0] azimuths. Streaky features confirm atomically flat surfaces.  $\delta$ -NbN and  $\gamma$ -Nb<sub>4</sub>N<sub>3</sub> exhibit (2 × 2) surface reconstructions, while  $\beta$ -Nb<sub>2</sub>N shows a (1 × 6) reconstruction.

comparable to previously reported high-quality films grown by MBE, highlighting the effectiveness of the atomically flat AlN templates. The crystalline quality of the NbN<sub>x</sub> films is fundamentally constrained by the structural anisotropy of the AlN template. The template's narrow out-of-plane tilt (10–12 arc sec) allows for nearly ideal vertical alignment, which is a prerequisite for the observation of pronounced Pendellösung fringes and the maintenance of atomically flat surface morphologies. Conversely, the broader in-plane twist of AlN (240–260 arc sec) establishes the baseline for the in-plane mosaicity of the NbN<sub>x</sub> layers. The NbN<sub>x</sub> films inherit and further expand this mosaic spread, as reflected in their in-plane FWHM values. No systematic dependence of XRC FWHM on film thickness (5–25 nm) was observed, suggesting that crystallinity remains largely thickness-independent within this range. This indicates that the epitaxial growth is stable across the investigated thickness range and that structural degradation with thickness is negligible. Overall, all NbN<sub>x</sub> phases exhibited narrow XRC widths indicative of high crystalline quality, with  $\gamma$ -Nb<sub>4</sub>N<sub>3</sub> showing slightly degraded in-plane coherence compared with  $\delta$ -NbN and  $\beta$ -Nb<sub>2</sub>N. Detailed thickness-dependent structural and superconducting parameters are summarized in Table S1 in the [supplementary material](#). The in-plane misorientation of  $\beta$ -Nb<sub>2</sub>N is primarily attributed to the lattice mismatch with the AlN template (−1.8%). Despite the hexagonal-on-hexagonal symmetry matching, this relatively significant mismatch promotes the formation of in-plane domain boundaries and mosaicity.

Reflection high-energy electron diffraction (RHEED) patterns (Fig. 2) were recorded along the AlN[112̄0] and [101̄0] azimuths for (a)  $\delta$ -NbN, (b)  $\gamma$ -Nb<sub>4</sub>N<sub>3</sub>, and (c)  $\beta$ -Nb<sub>2</sub>N. All films exhibited streaky features, confirming atomically flat surfaces. For  $\delta$ -NbN and  $\gamma$ -Nb<sub>4</sub>N<sub>3</sub>, half-order streaks were observed along both

azimuths, corresponding to a (2 × 2) surface reconstruction, which is commonly associated with the ordering of adatoms or vacancies on (111)-oriented nitride surfaces. Previous studies have shown that nitrogen loss from NbN surfaces can induce a (2 × 2) reconstruction, suggesting that such reconstructions may be related to nitrogen vacancy formation.<sup>33,34</sup> In contrast,  $\beta$ -Nb<sub>2</sub>N displayed one-sixth-order streaks along the AlN[101̄0] azimuth, indicative of a (1 × 6) reconstruction. While Katzer *et al.* reported a (2 × 2) reconstruction for MBE-grown  $\beta$ -Nb<sub>2</sub>N,<sup>14</sup> our observation of a (1 × 6) periodicity may reflect a different long-range ordering, possibly related to nitrogen vacancies or surface relaxation in sputter-deposited films on AlN. However, direct evidence of vacancy ordering is not available in the present study. The presence of these well-defined, phase-specific reconstructions provide compelling evidence of high crystalline quality and an atomically ordered surface, confirming a controlled epitaxial growth mode.

AFM images (Fig. 3) reveal the distinct surface morphologies of the AlN template and the epitaxial NbN<sub>x</sub> films. The AlN template [Fig. 3(a)] exhibited atomically flat step-and-terrace structures oriented along the AlN[1100] direction. Both  $\delta$ -NbN [Fig. 3(b)] and  $\gamma$ -Nb<sub>4</sub>N<sub>3</sub> [Fig. 3(c)] inherited this morphology, displaying triangular and inverted-triangular domains characteristic of twinned growth on AlN. This twinning arises from the symmetry mismatch between the threefold rotational symmetry of the cubic  $\delta$ -NbN (111) [or tetragonal  $\gamma$ -Nb<sub>4</sub>N<sub>3</sub>(112)] growth plane and the sixfold symmetry of the hexagonal AlN(0001) template. On such a surface, two distinct domain orientations rotated by 180° are energetically equivalent, leading to the nucleation of triangular grains pointing in opposite directions. Such twinning in  $\delta$ -NbN is consistent with previous reports,<sup>23</sup> while its occurrence in



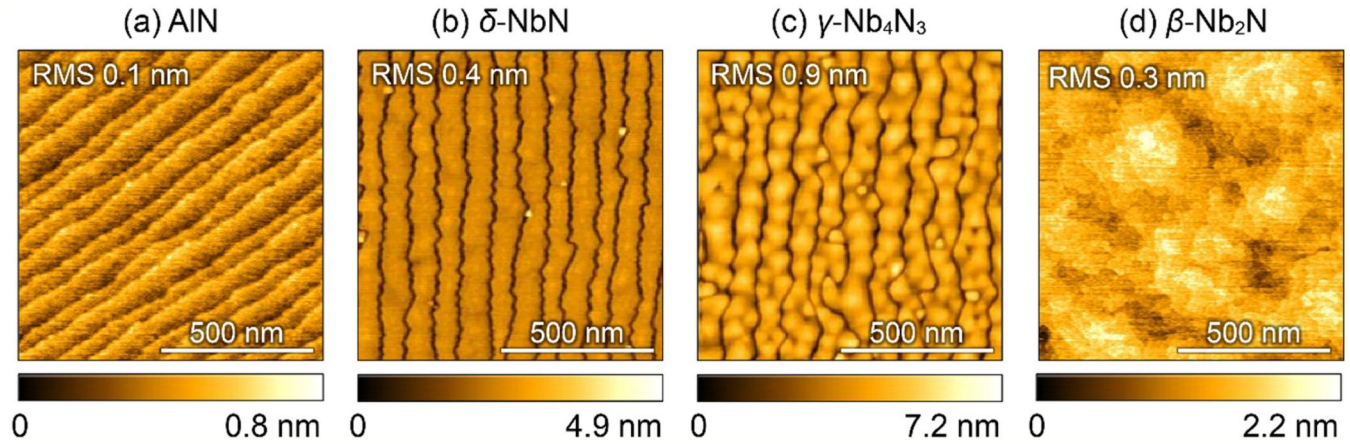


**FIG. 3.** AFM images of (a) AlN template, (b)  $\delta$ -NbN (10 nm), (c)  $\gamma$ -Nb<sub>4</sub>N<sub>3</sub> (15 nm), and (d)  $\beta$ -Nb<sub>2</sub>N (24 nm) films. All surfaces are atomically smooth with RMS roughness below 1 nm.

$\gamma$ -Nb<sub>4</sub>N<sub>3</sub> likely arises from the structural similarity between  $\delta$ -NbN (111) and  $\gamma$ -Nb<sub>4</sub>N<sub>3</sub> (112) growth planes. All NbN<sub>x</sub> films exhibited RMS roughness values below 1 nm, confirming their smooth surfaces. Among them,  $\beta$ -Nb<sub>2</sub>N showed the flattest morphology [Fig. 3(d)], which is attributed to the matching hexagonal crystal symmetry between  $\beta$ -Nb<sub>2</sub>N and the AlN substrate, which suppresses the formation of rotational twins. To further investigate the domain structures and the origin of the triangular features observed in AFM, azimuthal  $\varphi$ -scans were performed for off-axis reflections, such as the (002) reflection for  $\delta$ -NbN and (004) for  $\gamma$ -Nb<sub>4</sub>N<sub>3</sub>. As shown in Fig. S1 in the [supplementary material](#), these scans exhibit sixfold rotational symmetry instead of the threefold symmetry expected for a single-domain crystal. This result provides structural evidence for the formation of 180° rotational

twins, which arises from the symmetry mismatch between the epitaxial layers and the hexagonal AlN(0001) surface.

Reciprocal-space maps (RSMs) around the AlN(10 $\bar{1}$ 3) reflection (Fig. 4) confirm coherent growth of  $\delta$ -NbN (10 nm),  $\gamma$ -Nb<sub>4</sub>N<sub>3</sub> (6 nm), and  $\beta$ -Nb<sub>2</sub>N (24 nm), as evidenced by the coincidence of their  $q_x$  coordinates with that of AlN. For  $\gamma$ -Nb<sub>4</sub>N<sub>3</sub>, a single reciprocal lattice point was observed when grown coherently on AlN, whereas Wright *et al.*<sup>32</sup> reported two distinct reciprocal points for  $\gamma$ -Nb<sub>4</sub>N<sub>3</sub> grown on sapphire, attributed to a slight tetragonal distortion. This difference indicates that  $\gamma$ -Nb<sub>4</sub>N<sub>3</sub> grows on AlN in a  $\delta$ -NbN-like epitaxial mode. For  $\beta$ -Nb<sub>2</sub>N, coherent growth was maintained despite a large in-plane tensile strain of 1.8%, calculated from the bulk lattice constant ( $a = 0.3055$  nm<sup>14</sup>). This behavior suggests that the  $\beta$  phase may accommodate strain through

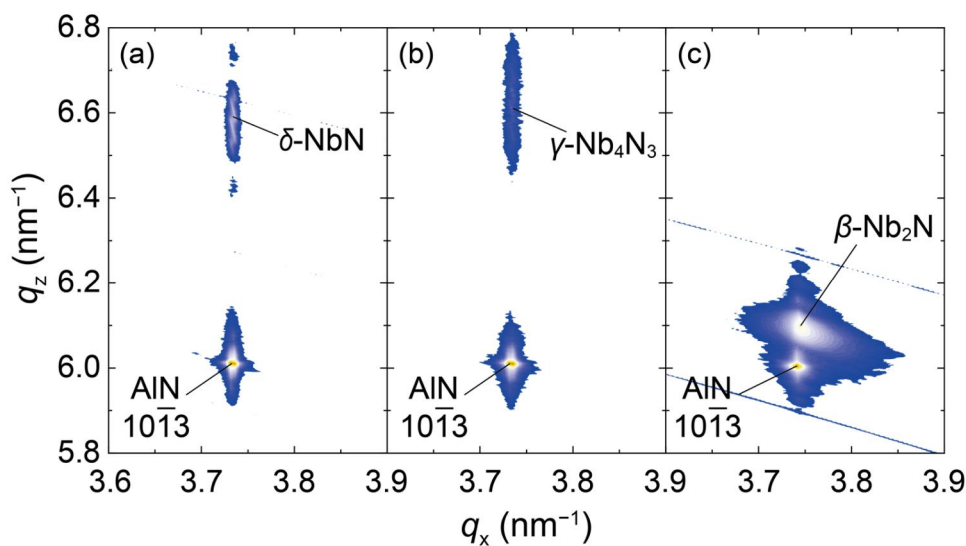


**FIG. 4.** RSMs around AlN(10 $\bar{1}$ 3) for (a)  $\delta$ -NbN (10 nm), (b)  $\gamma$ -Nb<sub>4</sub>N<sub>3</sub> (6 nm), and (c)  $\beta$ -Nb<sub>2</sub>N (24 nm) films grown on AlN/sapphire.

structural flexibility associated with the configurational freedom of nitrogen-site occupancy, which may contribute to the observed coherent growth despite the lattice mismatch. Specifically, in transition-metal nitrides, the nitrogen sublattice typically contains a significant concentration of vacancies. The redistribution of these nitrogen vacancies within the interstitial sites of the Nb sublattice allows the system to adjust its stoichiometry and unit-cell volume. This flexibility may contribute to the accommodation of strain under epitaxial constraint and thus to the observed coherent growth despite the lattice mismatch.<sup>24</sup> To quantify the structural properties, the lattice parameters of the epitaxial films were analyzed using both symmetric XRD and RSM measurements. The in-plane lattice parameters for all three phases were found to be constrained to that of the AlN template ( $a \approx 3.09 \text{ \AA}$ ). The experimental out-of-plane  $d$ -spacings for each phase were determined from the peak positions:  $d_{111} = 2.54 \text{ \AA}$  for  $\delta$ -NbN,  $d_{112} = 2.50 \text{ \AA}$  for  $\gamma$ -Nb<sub>4</sub>N<sub>3</sub>, and  $d_{0002} = 2.46 \text{ \AA}$  for  $\beta$ -Nb<sub>2</sub>N. These values, while slightly shifted from bulk standards due to the Poisson effect under the lattice-mismatched constraint, are consistent with the formation of phase-pure epitaxial layers as supported by RHEED analysis.

The superconducting transport properties of the NbN<sub>x</sub> thin films were systematically evaluated. Figure 5(a) shows the temperature dependence of the normalized resistance up to 300 K, while Fig. 5(b) presents an enlarged view of the superconducting transition region. The temperature-dependent behavior clearly varied with crystal phase.  $\delta$ -NbN exhibited an insulating-like resistivity upturn upon cooling. In contrast,  $\gamma$ -Nb<sub>4</sub>N<sub>3</sub> and  $\beta$ -Nb<sub>2</sub>N showed metallic conduction, with resistivity decreasing toward low temperature. The magnitude of the resistivity change differed among the phases, as reflected in the residual resistivity ratio (RRR), defined as  $R(300 \text{ K})/R(T \text{ just above } T_c)$ . The estimated RRR values were approximately 0.7 for  $\delta$ -NbN, 1.1 for  $\gamma$ -Nb<sub>4</sub>N<sub>3</sub>, and 1.7 for  $\beta$ -Nb<sub>2</sub>N. Because the low-temperature resistivity approaches the residual value determined by impurities and lattice defects, the larger RRR of  $\beta$ -Nb<sub>2</sub>N indicates higher crystalline purity and fewer scattering centers. To explain the temperature dependence of

resistivity in  $\delta$ -NbN, we consider the model proposed by Treece *et al.*,<sup>35</sup> which assumes that the film is composed of metallic NbN grains encased in an insulating Nb<sub>3</sub>N<sub>4</sub> shell. Under the nitrogen-rich growth conditions used for the  $\delta$  phase, the formation of such resistive Nb<sub>3</sub>N<sub>4</sub> inclusions at grain boundaries may dominate the transport behavior at low temperatures, resulting in the observed “insulating-like” resistivity upturn prior to the superconducting transition. The superconducting transition temperature  $T_c$  also varied systematically with phase:  $\sim 12 \text{ K}$  for  $\delta$ -NbN,  $\sim 10 \text{ K}$  for  $\gamma$ -Nb<sub>4</sub>N<sub>3</sub>, and  $0.4 \text{ K}$  for  $\beta$ -Nb<sub>2</sub>N.  $T_c$  was defined using the 50% criterion of the normal-state resistance.  $\delta$ -NbN consistently exhibited the highest  $T_c$ , whereas  $\beta$ -Nb<sub>2</sub>N showed the lowest, consistent with previous reports.<sup>24,32</sup> The phase purity of the  $\beta$ -Nb<sub>2</sub>N films is supported by the absence of superconducting signatures above  $1 \text{ K}$ , although the presence of minor secondary phases cannot be completely ruled out due to the absence of direct structural confirmation. Given that the  $\delta$  and  $\gamma$  phases possess  $T_c$  values an order of magnitude higher, their presence as secondary phases would likely trigger a detectable resistance drop at higher temperatures.

The observed variations in  $T_c$ —ranging from  $\sim 12 \text{ K}$  for  $\delta$ -NbN to  $\sim 0.4 \text{ K}$  for  $\beta$ -Nb<sub>2</sub>N—can be understood by structural symmetry and nitrogen stoichiometry.<sup>1</sup> The  $\delta$  phase, characterized by a symmetric rocksalt structure and high nitrogen content, facilitates a high electronic density of states at the Fermi level and robust electron–phonon coupling, leading to the highest  $T_c$  among the polymorphs. In contrast, the hexagonal  $\beta$  phase exhibits a significantly lower  $T_c$  due to its reduced nitrogen concentration and lower crystalline symmetry, which alters the Fermi surface topology. The metallic conduction observed in our  $\beta$ -Nb<sub>2</sub>N films down to  $0.4 \text{ K}$  further underscores the high phase purity achieved through our sputter epitaxy process.

The superconducting upper critical fields  $H_{C2}$  of  $\delta$ -NbN and  $\gamma$ -Nb<sub>4</sub>N<sub>3</sub> thin films were evaluated using a PPMS equipped with a 0–14 T superconducting magnet. The magnetic field orientation (parallel or perpendicular to the film plane) was controlled by rotating the sample stage. The temperature-dependent resistance was normalized to the normal-state resistance at  $50 \text{ K}$  ( $R_{50}$ ),

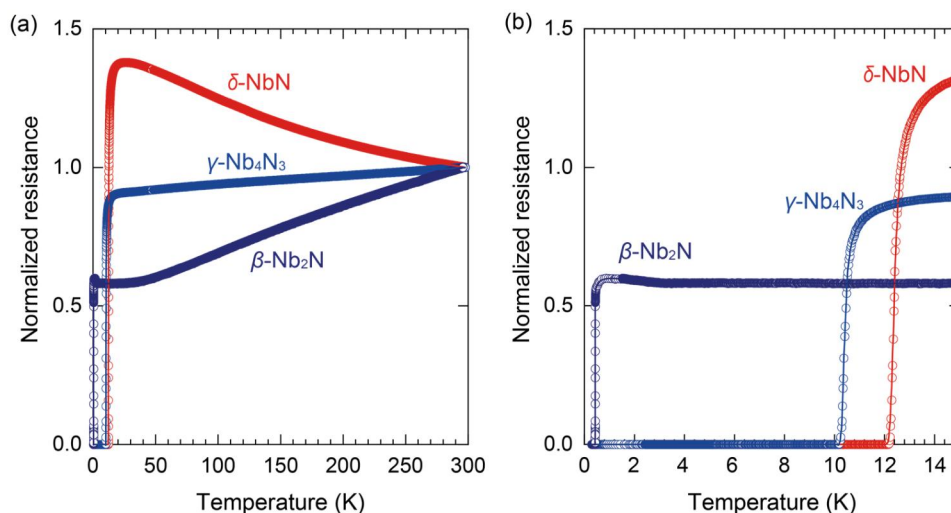


**FIG. 5.** Temperature-dependent normalized resistance of  $\delta$ -NbN,  $\gamma$ -Nb<sub>4</sub>N<sub>3</sub>, and  $\beta$ -Nb<sub>2</sub>N thin films grown on AlN/sapphire. (a) Full temperature range up to 300 K, illustrating phase-dependent metallic and insulating behaviors. (b) Enlarged view of the superconducting transition region, with  $T_c$  determined using the 50% criterion of the normal-state resistance.

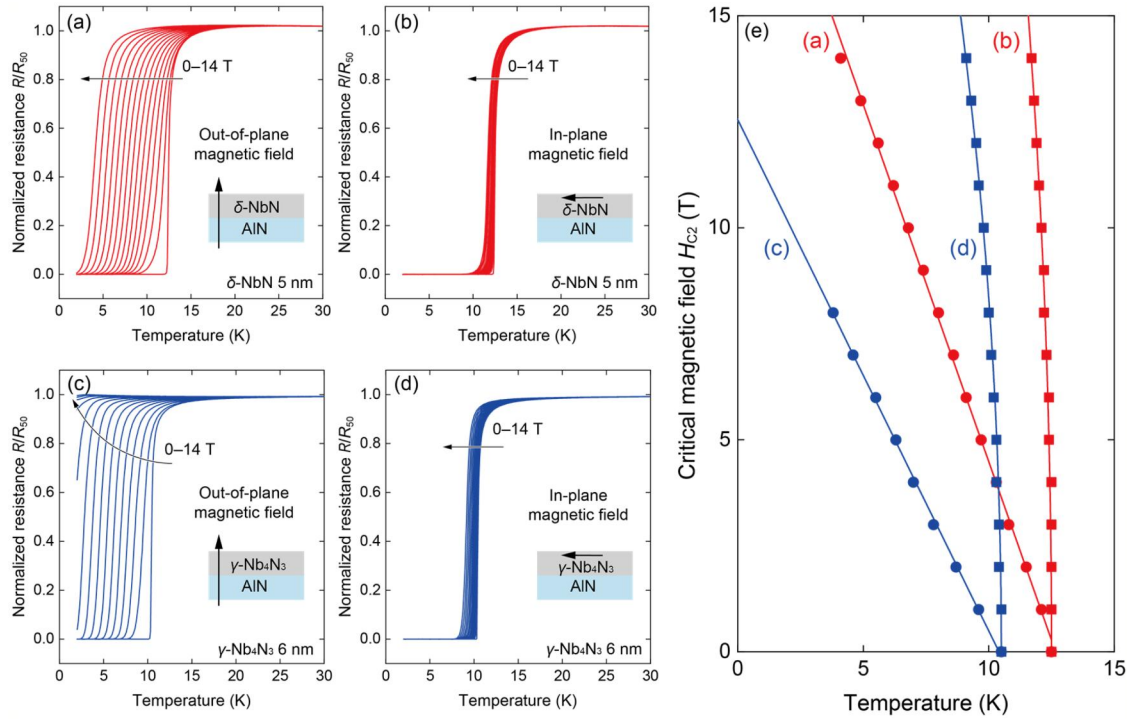


**FIG. 6.** Temperature-dependent normalized resistance ( $R/R_{50}$ ) of 5 nm-thick  $\delta$ -NbN and 6 nm-thick  $\gamma$ -Nb<sub>4</sub>N<sub>3</sub> thin films under magnetic fields applied perpendicular and parallel to the film plane.  $\delta$ -NbN [(a) and (b)] and  $\gamma$ -Nb<sub>4</sub>N<sub>3</sub> [(c) and (d)] films measured under 0–14 T. The in-plane field exhibits weaker suppression of  $T_c$  than the perpendicular field, indicating strong anisotropy in the upper critical field. (e) Plots of  $T_c$  vs critical magnetic field with Ginzburg–Landau fittings.

corresponding to the fully normal conducting state for all samples. Figure 6 shows the temperature-dependent normalized resistance  $R/R_{50K}$  of a 5 nm-thick  $\delta$ -NbN film [Figs. 6(a) and 6(b)] and a 6 nm-thick  $\gamma$ -Nb<sub>4</sub>N<sub>3</sub> film [Figs. 6(c) and 6(d)] under magnetic fields applied perpendicular and parallel to the film plane, respectively. Given their nearly identical thicknesses, these two samples provide a direct comparison of the phase-dependent anisotropy in the 2D limit.  $T_c$  decreased with increasing magnetic field, with a weaker suppression for the in-plane field, indicating pronounced anisotropy in the upper critical field. Figure 6(e) summarizes the relationship between  $T_c$  and the applied magnetic field for  $\delta$ -NbN and  $\gamma$ -Nb<sub>4</sub>N<sub>3</sub> films in both field orientations. The experimental data near  $T_c$  were fitted using the Ginzburg–Landau (GL) model for anisotropic superconductors.<sup>27</sup>

$$H_{c2}^{\perp}(T) = \frac{\Phi_0}{2\pi\zeta^2} \left(1 - \frac{T}{T_c}\right), \quad (1)$$

$$H_{c2}^{\parallel}(T) = \frac{\sqrt{12}\Phi_0}{2\pi\zeta d} \left(1 - \frac{T}{T_c}\right)^{\frac{1}{2}}, \quad (2)$$

where  $H_{c2}^{\perp}(T)$  and  $H_{c2}^{\parallel}(T)$  are the upper critical fields for magnetic fields applied perpendicular and parallel to the film plane,

respectively.  $\Phi_0 = h/2e$  is the magnetic flux quantum,  $\zeta$  is the GL coherence length at zero temperature,  $d$  is the superconducting film thickness, and  $T_c$  is the zero-field transition temperature. The zero-temperature upper critical fields,  $H_{c2}^{\perp}(0)$  and  $H_{c2}^{\parallel}(0)$ , are defined as the  $T \rightarrow 0$  limits of these expressions, i.e.,  $H_{c2}^{\perp}(0) = \Phi_0/(2\pi\zeta^2)$  and  $H_{c2}^{\parallel}(0) = \sqrt{12}\Phi_0/(2\pi\zeta d)$ , and were experimentally determined by extrapolating the fitted curves to  $T = 0$ . The fitting yielded  $H_{c2}^{\perp}(0)$  values of approximately 21 T for  $\delta$ -NbN and a smaller value of 13 T for the  $\gamma$ -Nb<sub>4</sub>N<sub>3</sub> film. The corresponding GL coherence lengths ( $\zeta$ ) were estimated to be approximately 4 nm for  $\delta$ -NbN and 5 nm for  $\gamma$ -Nb<sub>4</sub>N<sub>3</sub>, both smaller than their respective film thicknesses. The in-plane upper critical field  $H_{c2}^{\parallel}(0)$  reached 55 T for the  $\delta$ -NbN film and approximately 38 T for the  $\gamma$ -Nb<sub>4</sub>N<sub>3</sub> film, indicating that  $\delta$ -NbN possesses a higher tolerance to in-plane magnetic fields. For the 25 nm-thick  $\gamma$ -Nb<sub>4</sub>N<sub>3</sub> film, similar measurements were conducted under magnetic fields applied parallel and perpendicular to the film plane. Superconductivity was suppressed at relatively low magnetic fields of  $\sim 4$  T (perpendicular) and  $\sim 6$  T (parallel). While the degree of anisotropy is reduced compared to the ultrathin films, the distinct difference between the two orientations indicates that the film is in a dimensionality crossover regime. For the 25 nm-thick  $\gamma$ -Nb<sub>4</sub>N<sub>3</sub> film, this reduced anisotropy reflects a crossover from the ultrathin regime toward more three-dimensional superconducting

behavior. In this regime, the observed anisotropic behavior is still described within the framework of the GL model. The extracted  $\zeta$  for our films are summarized in Table S2 in the [supplementary material](#), alongside reported values for various NbN<sub>x</sub> polymorphs on different substrates. For the  $\delta$ -NbN phase, we obtained  $\zeta \approx 3.9$  nm, which is consistent with values reported for sputtered films on MgO (4.3–5.0 nm) and sapphire (4–6 nm). The larger  $\zeta$  ( $\sim 11$  nm) observed in some MBE-grown films on SiC may be related to their relatively lower  $H_{c2}(0)$  and  $T_c$  values compared to our sputtered films, as  $\zeta$  is inversely proportional to the square root of  $H_{c2}(0)$  in the Ginzburg–Landau framework.

#### IV. CONCLUSIONS

In summary, we achieved the phase-selective sputter epitaxy of  $\delta$ -NbN,  $\gamma$ -Nb<sub>4</sub>N<sub>3</sub>, and  $\beta$ -Nb<sub>2</sub>N thin films on atomically flat AlN templates. All NbN<sub>x</sub> phases exhibited coherent epitaxial growth with atomically smooth surfaces and high crystalline quality. Superconducting transport measurements revealed distinct phase-dependent characteristics, with  $T_c \approx 12$  K for  $\delta$ -NbN,  $\approx 10$  K for  $\gamma$ -Nb<sub>4</sub>N<sub>3</sub>, and 0.4 K for  $\beta$ -Nb<sub>2</sub>N. High-field measurements showed pronounced anisotropy of the upper critical field in ultrathin  $\delta$ -NbN and  $\gamma$ -Nb<sub>4</sub>N<sub>3</sub> films, whereas thicker  $\gamma$ -Nb<sub>4</sub>N<sub>3</sub> displayed nearly isotropic behavior. This thickness-dependent evolution of  $H_{c2}$  highlights the role of dimensionality in determining the superconducting properties of NbN<sub>x</sub>. These results define the growth windows and superconducting properties of NbN<sub>x</sub> polymorphs on AlN and provide key insights into phase stability, strain accommodation, and dimensional effects in transition-metal nitride superconductors. The demonstrated structural and superconducting compatibility between NbN<sub>x</sub> and III-nitride semiconductors establishes a solid foundation for future hybrid quantum and electronic devices that integrate superconductivity with wide-bandgap functionality.

#### SUPPLEMENTARY MATERIAL

See the [supplementary material](#) for additional structural and superconducting data. Figure S1 presents azimuthal  $\phi$ -scans of off-axis XRD reflections for  $\delta$ -NbN and  $\gamma$ -Nb<sub>4</sub>N<sub>3</sub> films, providing evidence of rotational twinning. Table S1 contains a comprehensive comparison of the structural properties, specifically the XRC FWHM, of  $\delta$ -NbN,  $\gamma$ -Nb<sub>4</sub>N<sub>3</sub>, and  $\beta$ -Nb<sub>2</sub>N thin films with previously reported values. Furthermore, Table S2 offers a comparison of superconducting parameters, including upper critical fields and Ginzburg–Landau coherence lengths, between this work and the existing literature.

#### ACKNOWLEDGMENTS

This work was partially supported by JSPS KAKENHI (Grant Nos. JP23KK0094, JP25K22019, and JP25K01680), the Izumi Science and Technology Foundation, the Foundation for Promotion of Material Science and Technology of Japan (MST Foundation), and the Research Foundation for the Electrotechnology of Chubu.

#### AUTHOR DECLARATIONS

##### Conflict of Interest

The authors have no conflicts to disclose.

##### Author Contributions

**Yuki Kato:** Data curation (lead); Formal analysis (equal); Resources (equal); Validation (equal); Visualization (equal); Writing – original draft (lead); Writing – review & editing (equal). **Koryo Masuzawa:** Data curation (supporting). **Takayuki Harada:** Data curation (supporting); Formal analysis (supporting); Validation (equal); Visualization (equal); Writing – review & editing (equal). **Hideto Miyake:** Data curation (supporting); Formal analysis (supporting); Validation (equal); Visualization (equal); Writing – review & editing (equal). **Atsushi Kobayashi:** Conceptualization (lead); Data curation (equal); Formal analysis (equal); Funding acquisition (lead); Project administration (lead); Resources (equal); Supervision (lead); Validation (equal); Visualization (equal); Writing – original draft (equal); Writing – review & editing (lead).

##### DATA AVAILABILITY

The data that support the findings of this study are available from the corresponding author upon reasonable request.

#### REFERENCES

- 1K. R. Babu and G.-Y. Guo, “Electron-phonon coupling, superconductivity, and nontrivial band topology in NbN polytypes,” *Phys. Rev. B* **99**(10), 104508 (2019).
- 2A. Semenov, B. Günther, U. Böttger, H.-W. Hübers, H. Bartolf, A. Engel, A. Schilling, K. Ilin, M. Siegel, R. Schneider, D. Gerthsen, and N. A. Gippius, “Optical and transport properties of ultrathin NbN films and nanostructures,” *Phys. Rev. B* **80**(5), 054510 (2009).
- 3W. Huang, “Thermodynamic assessment of the Nb–N system,” *Metall. Mater. Trans. A* **27**(11), 3591–3600 (1996).
- 4Y. Zou, X. Qi, C. Zhang, S. Ma, W. Zhang, Y. Li, T. Chen, X. Wang, Z. Chen, D. Welch, P. Zhu, B. Liu, Q. Li, T. Cui, and B. Li, “Discovery of superconductivity in hard hexagonal  $\epsilon$ -NbN,” *Sci. Rep.* **6**, 22330 (2016).
- 5J. Li, J. Li, W. Yi, M. Yin, Y. Fu, and G. Xi, “A metallic niobium nitride with open nanocavities for surface-enhanced Raman spectroscopy,” *Anal. Chem.* **94**(42), 14635–14641 (2022).
- 6Y. Nakamura, H. Terai, K. Inomata, T. Yamamoto, W. Qiu, and Z. Wang, “Superconducting qubits consisting of epitaxially grown NbN/AlN/NbN Josephson junctions,” *Appl. Phys. Lett.* **99**(21), 212502 (2011).
- 7S. Kim, H. Terai, T. Yamashita, W. Qiu, T. Fuse, F. Yoshihara, S. Ashhab, K. Inomata, and K. Semba, “Enhanced coherence of all-nitride superconducting qubits epitaxially grown on silicon substrate,” *Commun. Mater.* **2**(1), 98 (2021).
- 8R. Cheng, J. Wright, H. G. Xing, D. Jena, and H. X. Tang, “Epitaxial niobium nitride superconducting nanowire single-photon detectors,” *Appl. Phys. Lett.* **117**(13), 132601 (2020).
- 9Y. Pan, H. Zhou, X. Zhang, H. Yu, L. Zhang, M. Si, H. Li, L. You, and Z. Wang, “Mid-infrared Nb<sub>4</sub>N<sub>3</sub>-based superconducting nanowire single photon detectors for wavelengths up to 10  $\mu$ m,” *Opt. Express* **30**(22), 40044 (2022).
- 10I. Tret'yakov, S. Ryabchun, M. Finkel, A. Maslennikova, N. Kaurava, A. Lobastova, B. Voronov, and G. Gol'tsman, “Low noise and wide bandwidth of NbN hot-electron bolometer mixers,” *Appl. Phys. Lett.* **98**(3), 033507 (2011).



- <sup>11</sup>A. Shurakov, Y. Lobanov, and G. Goltsman, "Superconducting hot-electron bolometer: From the discovery of hot-electron phenomena to practical applications," *Supercond. Sci. Technol.* **29**(2), 023001 (2016).
- <sup>12</sup>J. K. G. Aschermann, E. Friederich, and E. Justi, "Supraleitfähige Verbindungen mit extrem hohen Springtemperaturen," *Phys. Z.* **42**, 349 (1941).
- <sup>13</sup>J. Wright, C. Chang, D. Waters, F. Lupke, R. Feenstra, L. Raymond, R. Koscica, G. Khalsa, D. Muller, H. G. Xing, and D. Jena, "Unexplored MBE growth mode reveals new properties of superconducting NbN," *Phys. Rev. Mater.* **5**(2), 024802 (2021).
- <sup>14</sup>D. S. Katzer, N. Nepal, D. J. Meyer, B. P. Downey, V. D. Wheeler, D. F. Storm, and M. T. Hardy, "Epitaxial metallic  $\beta$ -Nb<sub>2</sub>N films grown by MBE on hexagonal SiC substrates," *Appl. Phys. Express* **8**, 085501 (2015).
- <sup>15</sup>S. Kalal, A. Tayal, S. Karmakar, R. Joshi, R. Rawat, and M. Gupta, "Electron-phonon interactions and superconductivity of  $\beta$ -Nb<sub>2</sub>N thin films," *Appl. Phys. Lett.* **122**(7), 072602 (2023).
- <sup>16</sup>J. Yao, T. Li, A. Zhi, J. Ding, R. Xu, Y. Wang, Z. Zhao, Z. Liu, D. Shen, X. Tian, X. Bai, D. Feng, and J. Jiang, "Crystal and electronic structure of  $\beta$ -Nb<sub>2</sub>N thin films grown by molecular beam epitaxy," *Adv. Funct. Mater.* **35**(12), 2417638 (2025).
- <sup>17</sup>R. Sanjinés, M. Benkahoul, C. S. Sandu, P. E. Schmid, and F. Lévy, "Electronic states and physical properties of hexagonal  $\beta$ -Nb<sub>2</sub>N and  $\delta'$ -NbN nitrides," *Thin Solid Films* **494**(1–2), 190–195 (2006).
- <sup>18</sup>G.-I. Oya and Y. Onodera, "Transition temperatures and crystal structures of single-crystal and polycrystalline NbN<sub>x</sub> films," *J. Appl. Phys.* **45**(3), 1389–1397 (1974).
- <sup>19</sup>M. Tonouchi, Y. Sakaguchi, and T. Kobayashi, "Epitaxial growth of NbN on an ultrathin MgO/semiconductor system," *J. Appl. Phys.* **62**(3), 961–966 (1987).
- <sup>20</sup>S. P. Chockalingam, M. Chand, J. Jesudasan, V. Tripathi, and P. Raychaudhuri, "Superconducting properties and Hall effect of epitaxial NbN thin films," *Phys. Rev. B* **77**(21), 214503 (2008).
- <sup>21</sup>H.-W. Chang, V. K. Ranganayakulu, S.-Y. Guan, P.-J. Chen, M.-N. Ou, Y.-Y. Chen, T.-M. Chuang, C.-S. Chang, M.-K. Wu, and M.-J. Wang, "Superconducting (111)-orientated  $\delta$ -NbN epitaxial films on 4H-SiC substrates," *Supercond. Sci. Technol.* **34**, 045019 (2021).
- <sup>22</sup>J. R. Gao, M. Hajenius, F. D. Tichelaar, T. M. Klapwijk, B. Voronov, E. Grishin, G. Gol'tsman, C. A. Zorman, and M. Mehregany, "Monocrystalline NbN nanofilms on a 3C-SiC/Si substrate," *Appl. Phys. Lett.* **91**(6), 062504 (2007).
- <sup>23</sup>A. Kobayashi, K. Ueno, and H. Fujioka, "Autonomous growth of NbN nanostructures on atomically flat AlN surfaces," *Appl. Phys. Lett.* **117**(23), 231601 (2020).
- <sup>24</sup>A. Kobayashi, S. Kihira, T. Takeda, M. Kobayashi, T. Harada, K. Ueno, and H. Fujioka, "Crystal-phase controlled epitaxial growth of NbN<sub>x</sub> superconductors on wide-bandgap AlN semiconductors," *Adv. Mater. Interfaces* **9**(31), 2201244 (2022).
- <sup>25</sup>D. Sam-Giao, S. Pouget, C. Bougerol, E. Monroy, A. Grimm, S. Jebari, M. Hofheinz, J.-M. Gérard, and V. Zwiller, "High-quality NbN nanofilms on a GaN/AlN heterostructure," *AIP Adv.* **4**(10), 107123 (2014).
- <sup>26</sup>J. G. Wright, C. S. Chang, D. A. Muller, H. G. Xing, and D. Jena, "Structural and electronic properties of NbN/GaN junctions grown by molecular beam epitaxy," *APL Mater.* **10**(5), 051103 (2022).
- <sup>27</sup>R. Yan, G. Khalsa, S. Vishwanath, Y. Han, J. Wright, S. Rouvimov, D. S. Katzer, N. Nepal, B. P. Downey, D. A. Muller, H. G. Xing, D. J. Meyer, and D. Jena, "GaN/NbN epitaxial semiconductor/superconductor heterostructures," *Nature* **555**(7695), 183–189 (2018).
- <sup>28</sup>T. Yu, J. Wright, G. Khalsa, B. Pamuk, C. S. Chang, Y. Matveyev, X. Wang, T. Schmitt, D. Feng, D. A. Muller, H. G. Xing, D. Jena, and V. N. Strocov, "Momentum-resolved electronic structure and band offsets in an epitaxial NbN/GaN superconductor/semiconductor heterojunction," *Sci. Adv.* **7**(52), eabi5833 (2021).
- <sup>29</sup>A. Lachowski, P. Wolny, K. Dybko, M. Chlipała, K. Nowakowski-Szkudlarek, M. Hajdel, M. Żak, A. Feduniewicz, M. Sawicka, W. Chromiński, E. Grzanka, and C. Skierbiszewski, "NbN-based Josephson junctions grown by plasma-assisted molecular beam epitaxy," *Commun. Mater.* **6**, 169 (2025).
- <sup>30</sup>P. Dang, G. Khalsa, C. S. Chang, D. S. Katzer, N. Nepal, B. P. Downey, V. D. Wheeler, A. Suslov, A. Xie, E. Beam, Y. Cao, C. Lee, D. A. Muller, H. G. Xing, D. J. Meyer, and D. Jena, "An all-epitaxial nitride heterostructure with concurrent quantum Hall effect and superconductivity," *Sci. Adv.* **7**(8), eabf1388 (2021).
- <sup>31</sup>H. Miyake, C.-H. Lin, K. Tokoro, and K. Hiramatsu, "Preparation of high-quality AlN on sapphire by high-temperature face-to-face annealing," *J. Cryst. Growth* **456**, 155–159 (2016).
- <sup>32</sup>J. G. Wright, H. G. Xing, and D. Jena, "Growth windows of epitaxial NbN<sub>x</sub> films on c-plane sapphire and their structural and superconducting properties," *Phys. Rev. Mater.* **7**(7), 074803 (2023).
- <sup>33</sup>G.-Y. Wang, Z. Zhu, X.-Y. Yang, L. Dong, H.-Y. Ma, H.-H. Sun, A.-M. Li, D.-D. Guan, D. Qian, C. Liu, Y.-Y. Li, and J.-F. Jia, "Atomically flat superconducting NbN thin films grown on SrTiO<sub>3</sub> (111) by plasma-assisted MBE," *APL Mater.* **5**(12), 126107 (2017).
- <sup>34</sup>J. Talvacchio, S. Sinharoy, and A. I. Braginski, "Surface stability of NbN single-crystal films," *J. Appl. Phys.* **62**(2), 611–614 (1987).
- <sup>35</sup>R. E. Treece, M. S. Osofsky, E. F. Skelton, S. B. Qadri, J. S. Horwitz, and D. B. Chrisey, "New phase of superconducting NbN stabilized by heteroepitaxial film growth," *Phys. Rev. B* **51**(14), 9356–9359 (1995).